Supporting Information

Mechanistic Origins of the High-Pressure Inhibition of Methanol Dehydration Rates in Small-Pore Acidic Zeolites

John R. Di Iorio,[1] Alexander J. Hoffman,[2] Claire T. Nimlos,[1] Steven Nystrom,[2] David Hibbitts,*[2] Rajamani Gounder*[1]

[1]*Charles D. Davidson School of Chemical Engineering, Purdue University, 480 Stadium Mall Drive, West Lafayette, IN 47907, USA*

[2]*Department of Chemical Engineering, University of Florida, 1030 Center Drive, Gainesville, FL 32611, USA*

*Corresponding author. E-mails: hibbitts@ufl.edu, rgounder@purdue.edu

Table of Contents

List of Figures, Tables, and Schemes

S.1. Statistical mechanics approximations for rate and equilibrium constants

Enthalpies (*H*) and free energies (*G*) for gas-phase and adsorbed species are calculated as a sum of DFT-calculated electronic energy (E_0), zero-point vibrational energy (ZPVE), and vibrational, translational, and rotational enthaplies (H_{vib}, H_{trans}, H_{rot}) and free energies (G_{vib}, G_{trans}, G_{rot}):

$$H = E_0 + ZPVE + H_{vib} + H_{trans} + H_{rot} \tag{S.1}$$

$$G = E_0 + ZPVE + G_{vib} + G_{trans} + G_{rot} \tag{S.2}$$

Motions of adsorbates within the zeolite framework were considered frustrated movements and only contributed to vibrational terms such that translational and rotational *H* and *G* were zero. Framework Al atoms and the four O atoms bound to them were included in normal mode analysis, but all remaining framework Si and O atoms remained static during frequency calculations. Vibrational, rotational, and translational energies were calculated from statistical mechanics [1]:

$$ZPVE = \sum_i \left(\frac{1}{2} h\nu_i\right) \tag{S.3}$$

$$H_{vib} = \sum_i \left(\frac{h\nu_i e^{\frac{-h\nu_i}{k_B T}}}{1-e^{\frac{-h\nu_i}{k_B T}}} \right) \tag{S.4}$$

$$G_{vib} = \sum_i \left(-k_B T \ln \left(\frac{1}{1-e^{\frac{-h\nu_i}{k_B T}}} \right) \right) \tag{S.5}$$

Translational and rotational free energies and enthalpies were calculated for all gas-phase species:

$$H_{trans} = \frac{5}{2} k_B T \tag{S.6}$$

$$H_{rot,linear} = k_B T \tag{S.7}$$

$$H_{rot,nonlinear} = \frac{3}{2} k_B T \tag{S.8}$$

$$G_{trans} = -k_B T \ln \left(\left(\frac{2\pi M k_B T}{h^2} \right)^{\frac{3}{2}} V \right) \tag{S.9}$$

$$G_{rot} = -k_B T \ln \left(\frac{\pi^{\frac{1}{2}}}{\sigma} \left(\frac{T^3}{\theta_x \theta_y \theta_z} \right)^{\frac{1}{2}} \right) \tag{S.10}$$

$$\theta_i = \frac{h^2}{8\pi^2 k_B I_i} \tag{S.11}$$

where I_i is the moment of inertial about each axis and σ is the symmetry number. Entropies (*S*) are calculated from *H* and *G*:

$$S = \frac{H-G}{T} \tag{S.12}$$

G values at a wide range of temperatures (300–500 K) were estimated from *H* and *S* values calculated at 415 K.

Rate constants can be approximated from DFT-calculated enthalpies and free energies at a range of temperatures using statistical mechanics formalisms:

$$k = \frac{k_B T}{h} \exp\left(\frac{-\Delta G^{\ddagger}}{k_B T}\right) \tag{S.13}$$

$$K = \exp\left(\frac{-\Delta G_{ads}}{k_B T}\right) \tag{S.14}$$

where k_B is Boltzmann's constant. Rate and equilibrium constants are calculated at standard pressures (1 bar CH_3OH).

S.2. Configurational effects on calculated energies for intermediates and transition states

The CHA framework has four distinct O atoms around its only unique T-site; these O atoms are show in Figure S.1 with the rings of the CHA framework. A proton (which can accommodate H-bound adsorbates), methyl group, or transition state can interact with each of these O atoms. This multiplicity of locations for binding lends itself to configurational complexity in theory approaches to studying zeolites. Moreover, the plethora of confining environments within zeolites—even those with high symmetry, such as CHA—further compounds this configurational complexity.

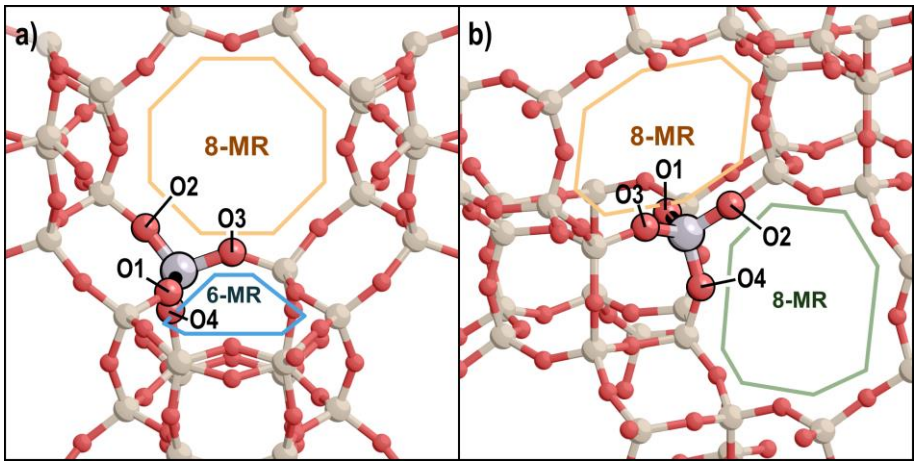

Figure S.1. CHA structure with Al substituted for a Si atom. Symmetrically unique O atoms around this Al atom are labeled from convention [2]. (a) The six-member (6-MR) and eight-member (8-MR) rings containing O1, O2, and O3 of the Al atom; (b) another view showing the two 8-MR shared by O2 of the Al containing O2, O3, and O4.

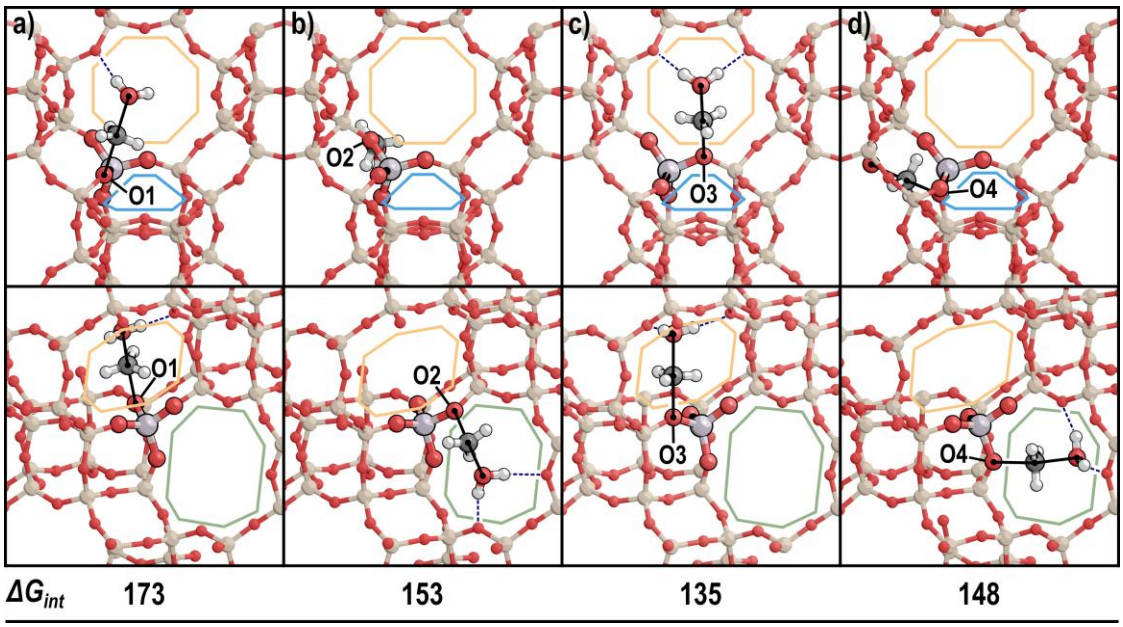

Figure S.2. The lowest energy transition states for the first step of the dissociative mechanism without spectators on (a) O1, (b) O2, (c) O3, and (d) O4. H-bonds are shown with blue dashed lines and incipient and breaking bonds are shown with black lines. The O atom with which the transition state is interacting is labeled. Intrinsic free energy barriers (ΔG_{int}) are shown in kJ mol^{-1} also relative to one adsorbed methanol.

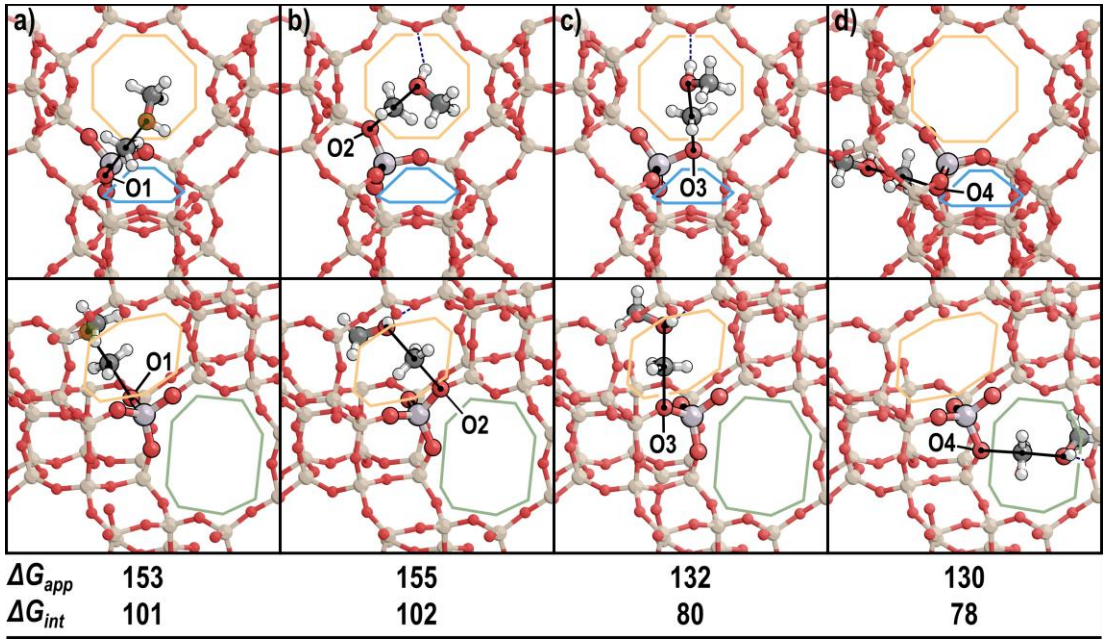

Figure S.3. The lowest energy transition states for the second step of the dissociative mechanism without spectators on (a) O1, (b) O2, (c) O3, and (d) O4. H-bonds are shown with blue dashed lines and incipient and breaking bonds are shown with black lines. The O atom with which the transition state is interacting is labeled. Apparent free energy (ΔG_{app}) barriers are shown in kJ mol^{-1} relative to one adsorbed methanol. Intrinsic free energy barriers (ΔG_{int}) are shown in kJ mol^{-1}.

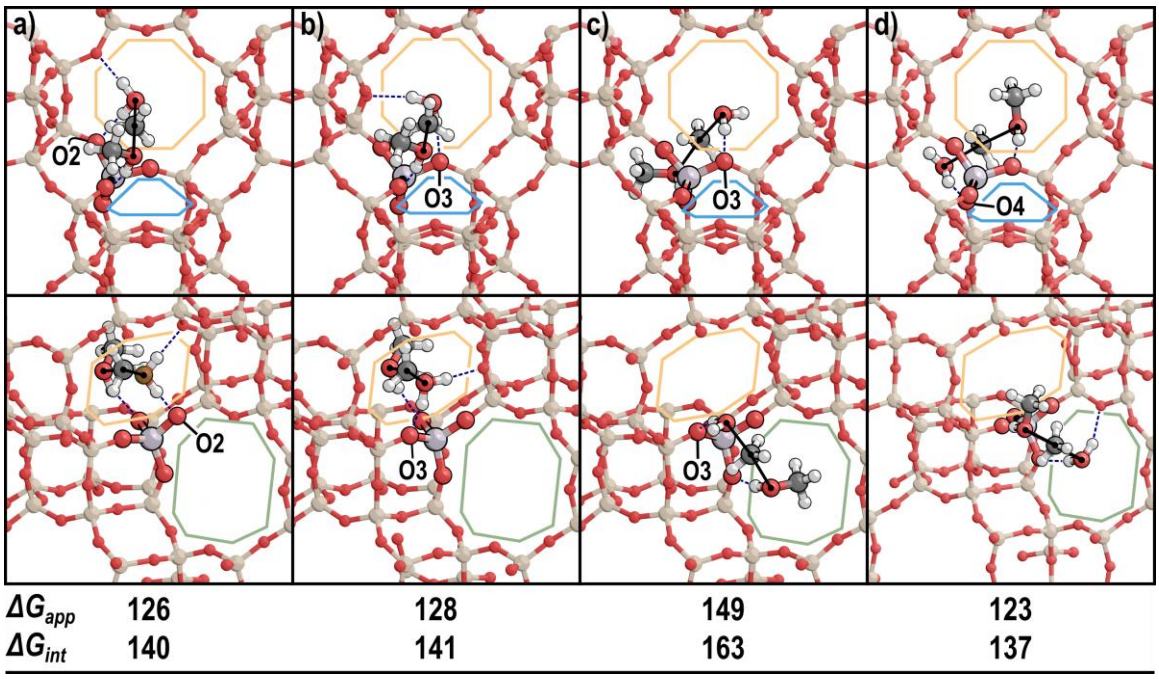

Figure S.4. The four lowest energy transition states for the associative mechanism without spectators with the with (a) the water H-bonding with O2 and methanol H-bonding with O1, (b) the water H-bonding with O3 and methanol H-bonding with O1, (c) the water H-bonding with O3 and methanol H-bonding with O4, and (d) the water H-bonding with O4 and methanol H-bonding with O3. H-bonds are shown with blue dashed lines and incipient and breaking bonds are shown with black lines. The O atom with which the water is interacting is labeled. Apparent free energy (ΔG_{app}) and enthalpic (ΔH_{app}) barriers are shown in kJ mol^{-1} and apparent entropies (ΔS_{app}) in J mol^{-1} K, relative to one adsorbed methanol. Intrinsic free energy barriers (ΔG_{int}) are shown in kJ mol^{-1} also relative to one adsorbed methanol.

S.3. Comparison of dissociative and associative mechanisms without spectating methanol molecules

Methanol dehydration, if it proceeds via the dissociative route, can be limited by either of the two steps in that pathway. The relative rates of the two pathways can be assessed by computing rates using a maximum rate analysis (as seen in Section 3.5 of the main text) or by comparing the forward and reverse reactions possible from a surface methyl group. A surface methyl group during methanol dehydration can either (1) react with water to re-form methanol or (2) react with another methanol to form dimethyl ether (DME) (Scheme S.1). Coefficients of adsorption in the presence of a CH_3–Z species for H_2O (K_{W-M}) and CH_3OH (K_{M-M}) define adsorption steps prior to reaction to form DME (k_{D2}) or to re-form methanol (k_{-D1}).

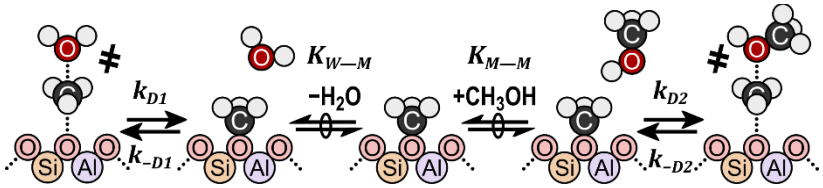

Scheme S.1. The possible routes to remove a surface methyl (CH_3–Z) group during methanol dehydration.

Based on the paths described in Scheme S.1, rate equations can be derived to describe the formation of methanol from this surface methyl:

$$r_{-D1} = k_{-D1} K_{W-M} P_{H_2O} \tag{S.15}$$

or to describe the formation of DME:

$$r_{D2} = k_{D2} K_{M-M} P_{CH_3OH} \tag{S.16}$$

The ratios of these rates can be written as a function of conversion (X) to compare the relative rates of these two steps and determine the rate-determining step (RDS) of the dissociative mechanism:

$$\frac{r_{-D1}}{r_{D2}} = \frac{k_{-D1} K_{W-M}}{k_{D2} K_{M-M}} \left(\frac{X}{1-X} \right) \tag{S.17}$$

Using energies calculated from DFT, these rate and equilibrium constants can be calculated from statistical mechanics formalisms (Section S.1) (415 K, 1 bar CH_3OH). Ultimately, the ratio of these rate and equilibrium coefficients reflects the difference in energy between the two transition states:

$$\frac{k_{-D1} K_{W-M}}{k_{D2} K_{M-M}} = \exp\left(\frac{-\left(\Delta G^{\ddagger}_{D1} - \Delta G^{\ddagger}_{D2} \right)}{k_B T} \right) \tag{S.18}$$

These calculated values were used to estimate the ratio of rates of methanol formation and DME formation from a CH_3–Z group at different conversions using Eq. S.17 (Fig. S.5). The rate of the second step of the dissociative mechanism exceeds the reverse rate of the first step by at least a factor of 10 at all conversions tested experimentally. This indicates that the first step of the dissociative route can be considered irreversible and is the RDS at all relevant catalytic conditions when spectating methanol species are excluded.

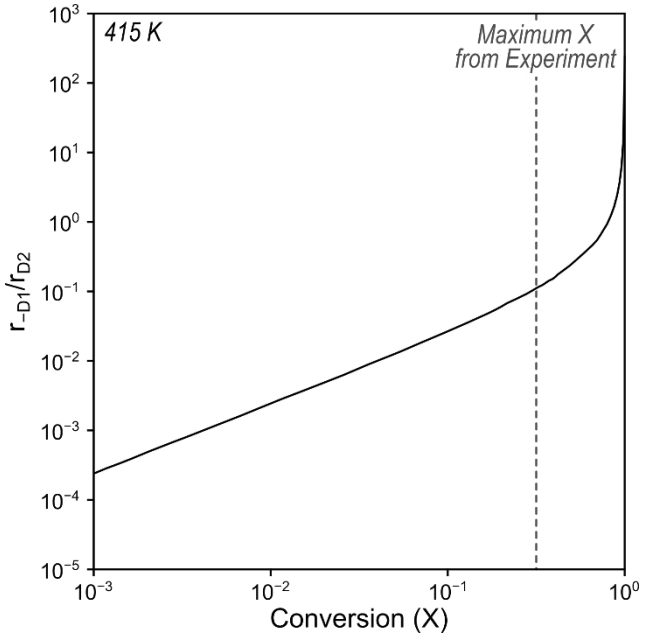

Figure S.5. Ratio of rates of the two possible rate-determining steps in dissociative methanol dehydration at 415 K. The maximum conversion tested experimentally is marked with a dashed line.

The relative rates of the dissociative mechanism (which is limited by its first step at relevant conditions) and the associative mechanism can be compared using maximum rate analysis. DFT-calculated enthalpies and entropies can be used to approximate rate and equilibrium constants at standard conditions (Section S.1), from which rates can be estimated using the appropriate rate equations. The rate equation for the dissociative mechanism without spectators and without considering anything larger than a methanol dimer as a most abundant surface intermediate (MASI) is:

$$r_{D1} = \frac{k_{D1} K_M P_M}{1 + K_M P_M + K_M K_D P_M^2} \tag{S.19}$$

The rate equation for the associative mechanism with the same assumptions is

$$r_A = \frac{k_A K_M K_D P_M^2}{1 + K_M P_M + K_M K_D P_M^2} \tag{S.20}$$

The ratio of these two rates, therefore, is

$$\frac{r_D}{r_A} = \frac{k_D}{k_A K_D P_M} \tag{S.21}$$

The ratio of these rate coefficients reflects the differences in free energy between the dissociative ($\Delta G_{D1}^{\ddagger}$) and associative ($\Delta G_A^{\ddagger}$) transition states and a methanol dimer structure (ΔG_D):

$$\frac{k_D}{k_A K_D} = \exp\left(-\frac{\left(\Delta G_{D1}^{\ddagger} - \Delta G_A^{\ddagger} - \Delta G_D\right)}{k_B T}\right) \tag{S.22}$$

The dissociative mechanism prevails at low methanol pressures, but the associative mechanism dominates at higher pressures (Fig. S.6). The pressure at which the prevalent mechanism shifts from dissociative to associative increases with increasing temperature. This reflects differences in

enthalpic and entropic contributions to relevant free energies; the associative mechanism is enthalpically favored but entropically disfavored as adsorption of additional methanol molecules results in entropic losses. This is consistent with previous work which has found a preference for the dissociative mechanism at elevated reaction temperatures in MFI [5] and on polyoxometalates [6] due to entropic contributions to the free energies for these mechanisms.

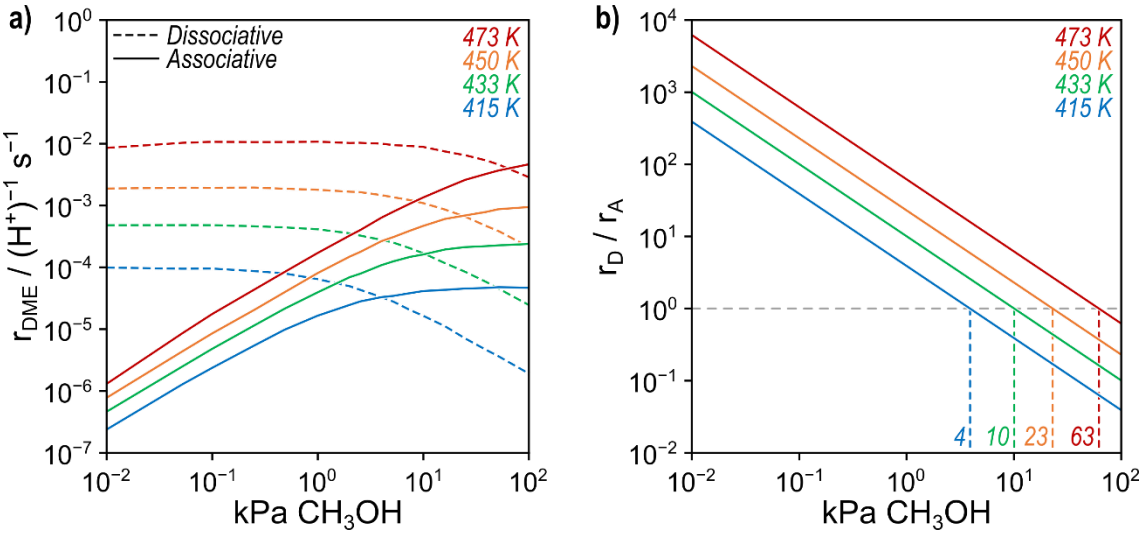

Figure S.6. (a) DFT-predicted rates of dissociative (dashed lines) and associative (solid lines) methanol dehydration without spectators and excluding intermediates larger than two methanol molecules at 415 K (blue), 433 K (green), 450 K (orange), and 473 K (red). (b) Ratios of the dissociative and associative rates of DME formation at these temperatures, with the pressures at which the prevailing route shifts from dissociative to associative labeled in kPa.

S.4. Purification and drying of reactant methanol

Additional water may also have entered the system via the reactant methanol and this was also considered as a possible source of water contamination. Methanol (99.9 wt%, HPLC-grade, Sigma-Aldrich) was further purified by first removing dissolved gases (e.g., N_2, O_2) via freeze-pump-thaw until the equilibrium vapor pressure of methanol at room temperature (13.6 kPa at ~294 K) was reached and no bubbling was observed upon thawing (an indication of volatile contaminants). After the freeze-pump-thaw cycles, methanol was then refluxed overnight (338 K) under an Ar atmosphere (99.999%, Indiana Oxygen) to minimize the presence of volatile organic contaminants (e.g., formaldehyde) [7]. Finally, methanol was then transferred via a double-ended cannula to a round-bottom flask containing dehydrated 3A molecular sieves (dried at 523 K under dynamic vacuum overnight (<5 Pa); Sigma-Aldrich) held under an Ar atmosphere and left overnight to remove residual water. This dried, degassed methanol was then transferred via gas-tight syringe, to the syringe pump and used as the reactant feed. Methanol dehydration rates (per H^+, 415 K) using this purified methanol are indistinguishable from those measured with unpurified methanol and are inhibited to a similar extent at high methanol pressures (>10 kPa; Fig. S.7).

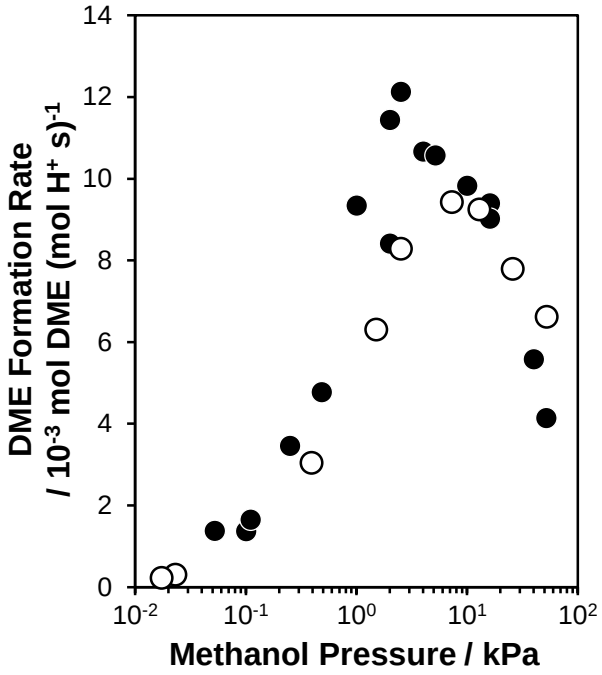

Figure S.7. DME formation rate (per H^+, 415 K) measured on H-CHA with only isolated H^+ sites as a function of methanol pressure using unpurified (solid) and purified methanol (open).

S.5. DFT-calculated methanol cluster stability

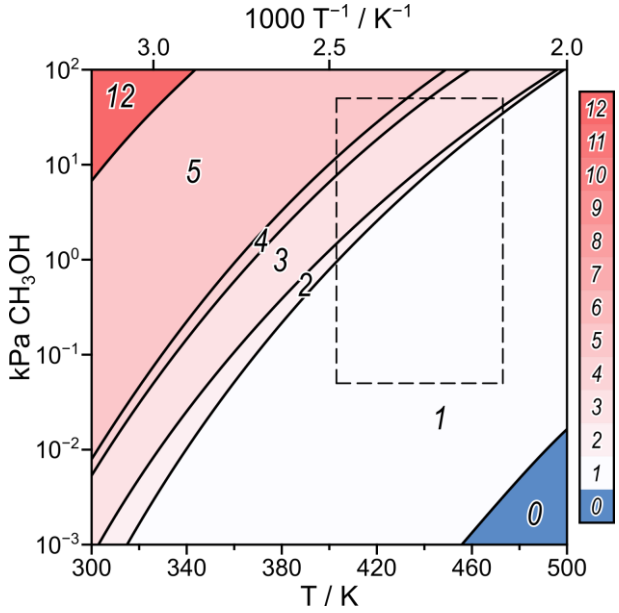

Figure S.8. Phase diagram predicting the most stable methanol cluster size at isolated H^+ sites in CHA, denoted by the phase boundary lines in the figure and the colored legend to the right of the figure. Equilibrium constants for adsorption were predicted by free energies from DFT at 415 K and 1 bar CH_3OH. The area enclosed by dashed lines correspond to the range of kinetic conditions studied for methanol dehydration in this work (403–473 K, 0.05–50 kPa CH_3OH).

S.6. ^{1}H NMR spectrum of 1,2-dimethyl-3-(4-methylbenzyl)imidazolium chloride

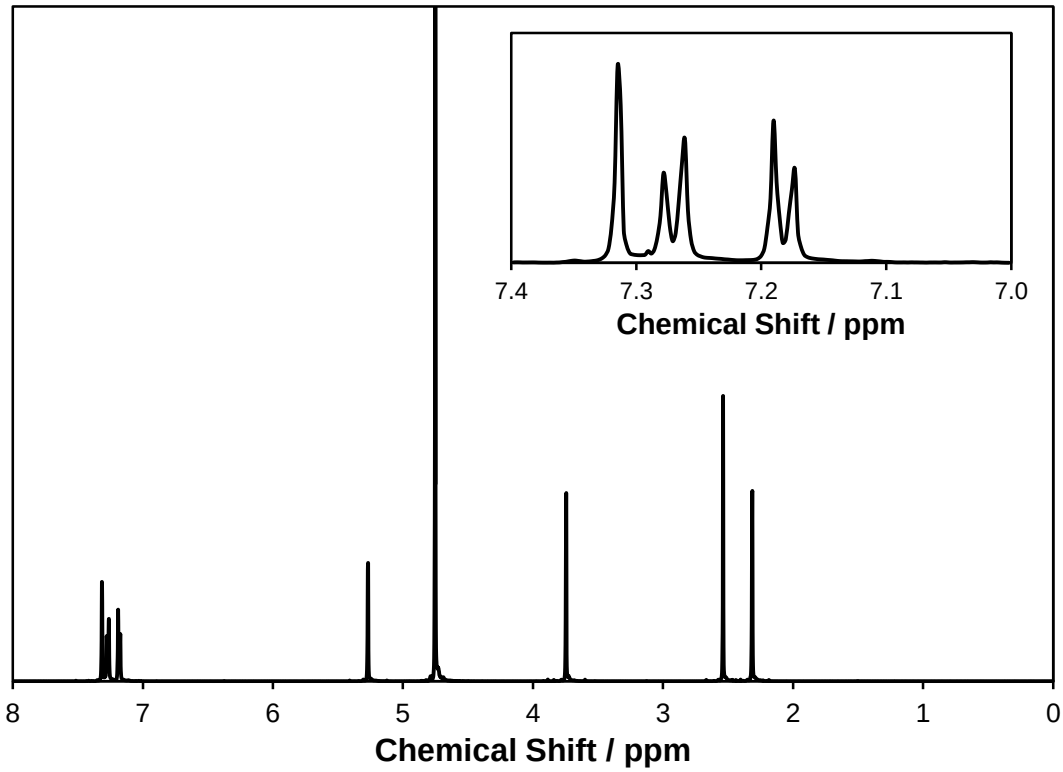

Figure S.9. ^{1}H NMR spectrum of 1,2-dimethyl-3-(4-methylbenzyl)imidazolium chloride in D_2O. Peak at ~4.7 ppm is due to residual H_2O present in the D_2O solvent. Inset shows a zoom in to the region between 7.4-7.0 ppm.

The overall reaction for the synthesis of 1,2-dimethyl-3-(4-methylbenzyl)imidazolium chloride is shown in Scheme S.2 and the assigned chemical shifts of each H atom of the product are shown in Scheme S.3. Notably, only a single resonance is observed for the two olefinic H atoms of the imidazolium ring (δ: 7.31 ppm; Fig. S.9, inset). Integration of this peak indicates that 2 H atoms share this chemical shift and is likely representative of a resonance structure of the delocalized imidazolium cation where the charge is shared across the N atoms (Scheme S.3) [8].

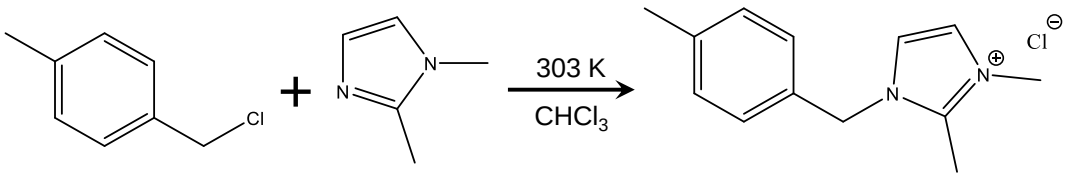

Scheme S.2. Overall reaction between 4-methylbenzyl chloride and 1,2-dimethylimidazole to form 1,2-dimethyl-3-(4-methylbenzyl)imidazolium chloride.

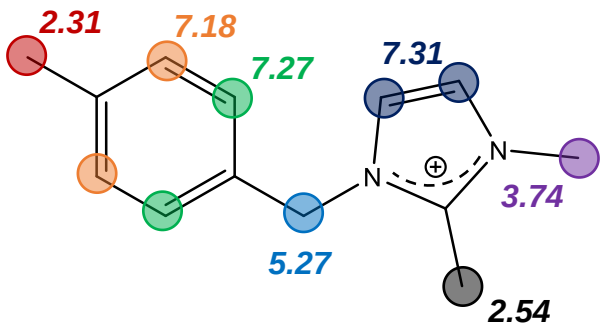

Scheme S.3. Proposed resonance structure of the imidazolium cation. Colored circles are used to distinguish chemically distinct H atoms (not shown) and their corresponding ^{1}H NMR chemical shifts (in ppm). ^{1}H NMR (D_2O, 500 MHz): δ 7.31 (s, 2H), 7.27 (d, 2H), 7.18 (d, 2H), 5.27 (s, 2H), 3.74 (s, 3H), 2.54 (s, 3H), 2.31 (s, 3H).

S.7. Powder X-ray diffraction patterns of different small-pore zeolites

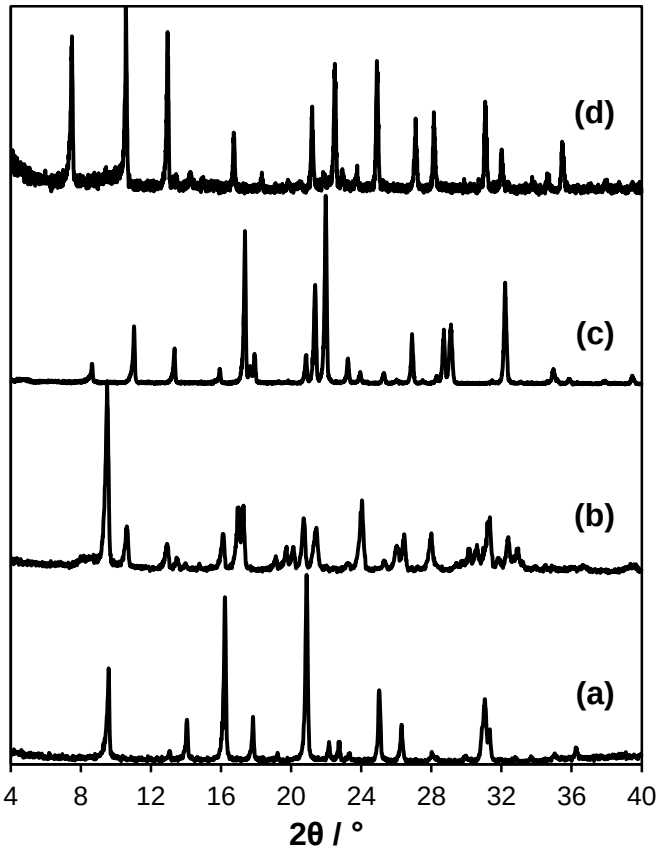

Figure S.10. Powder XRD patterns of (a) CHA, (b) AEI, (c) LEV, and (d) LTA zeolites.

S.8. Argon adsorption isotherms (87 K) on various small-pore zeolites

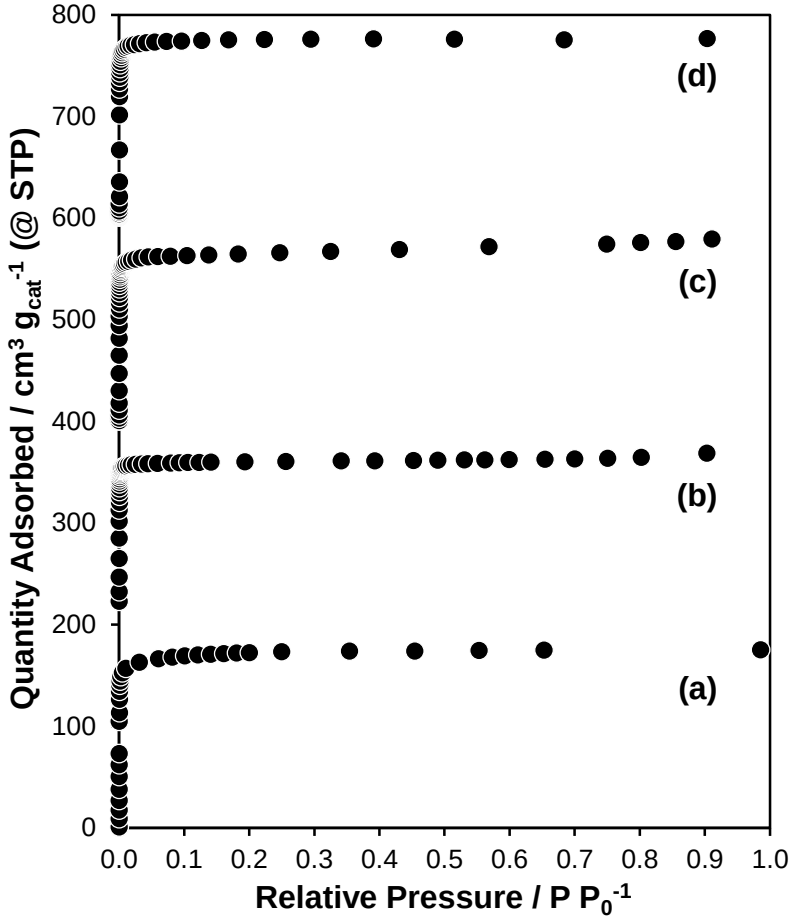

Figure S.11. Ar adsorption isotherms (87 K) measured on (a) CHA, (b) AEI, (c) LEV, and (d) LTA zeolites. Isotherms are vertically offset by 200 $cm^3\ g_{cat}^{-1}$.

S.9. Tabulated micropore volumes, Al content, and H^+ site content on different small-pore zeolites

Table S.1. Micropore volumes estimated from Ar adsorption isotherms (87 K), total Al content measured by AAS, and H^+ site contents measured by NH_3 TPD on different small-pore zeolites.

Zeolite Framework	Micropore Volume / $cm^3\ g_{cat}^{-1}$ (@ STP)	Al Content 10^{-3} mol Al g_{cat}^{-1}	Si/Al	H^+ Site Content 10^{-3} mol H^+ g_{cat}^{-1}	H^+/Al
LTA	0.21	0.57	28	0.46	0.81
CHA	0.19	0.98	16	0.93	0.95
AEI	0.20	1.59	9.5	1.35	0.85
LEV	0.20	0.98	16	0.93	0.95

S.10. Measurement of methanol dehydration activation enthalpies and entropies on CHA zeolites

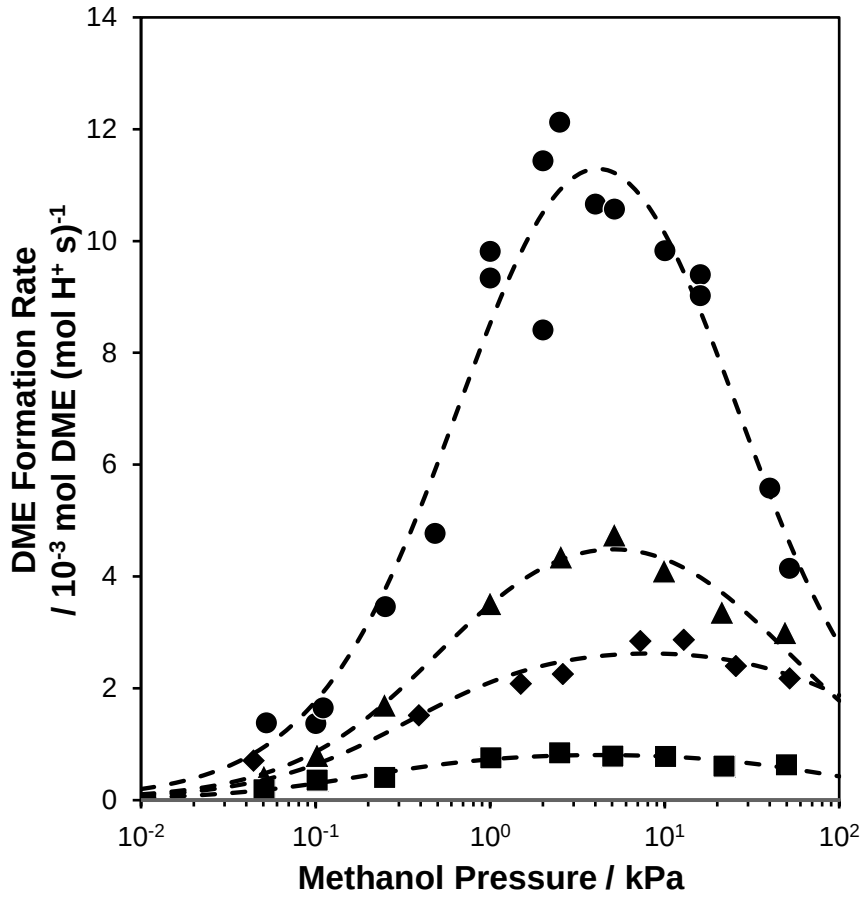

Figure S.12. DME formation rates measured as a function of methanol pressure at 383 (squares), 398 (diamonds), 403 (triangles), and 415 K (circles) on a CHA zeolite with only isolated H^+ sites. Dashed lines are least squares regressions to Eq. 4 (main text).

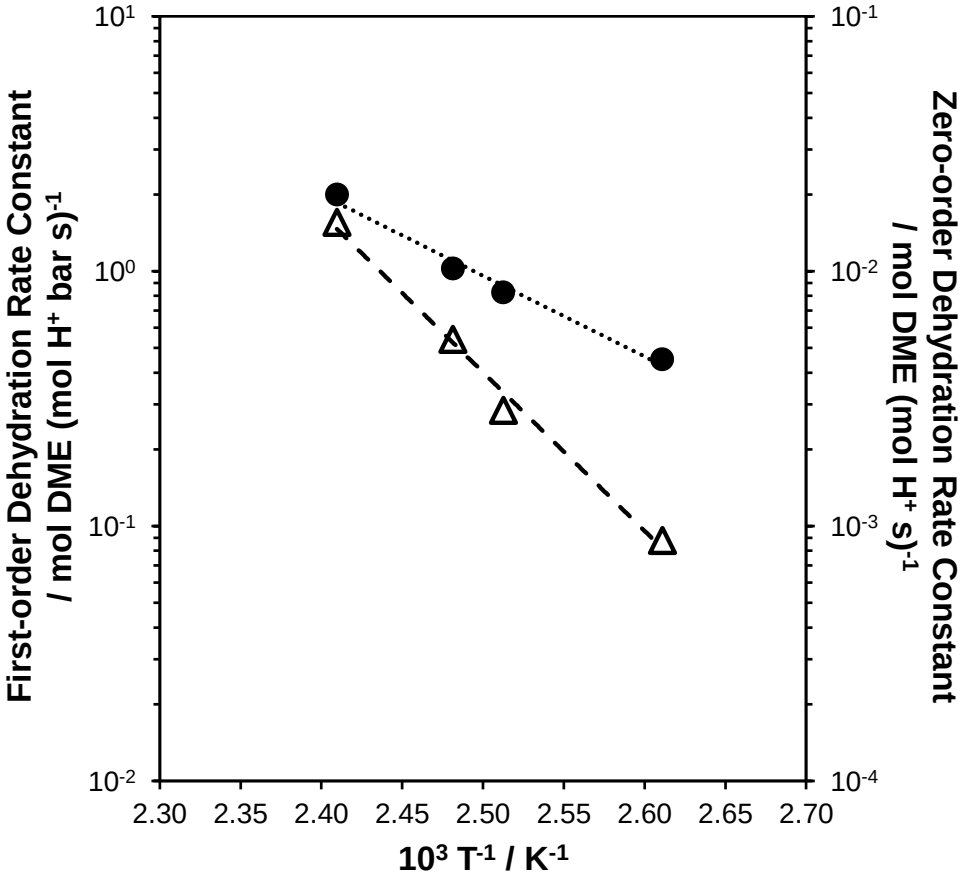

Figure S.13. First-order (circles) and zero-order (triangles) methanol dehydration rate constants (per H^+ site) measured as a function of temperature (383-415 K) on a CHA zeolite containing isolated H^+ sites.

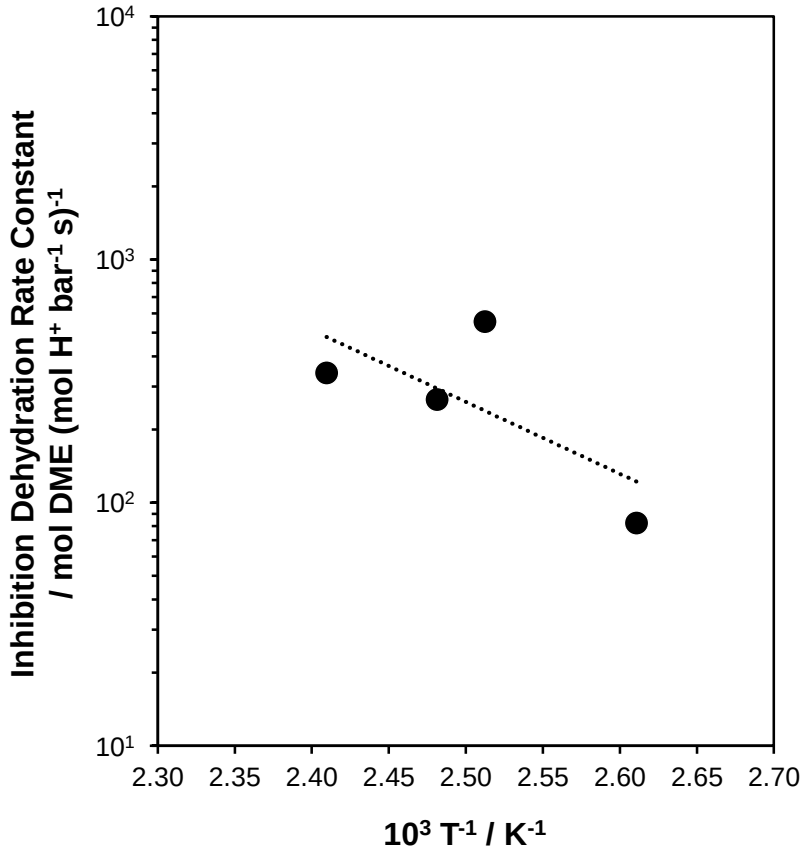

Figure S.14. Apparent inhibition methanol dehydration rate constant (per H^+ site) measured as a function of temperature (383-415 K) on a CHA zeolite containing only isolated H^+ sites.

First-order and zero-order apparent activation enthalpies and entropies were calculated from measured methanol dehydration rate constants (Fig. S.12 and S.13) using the Eyring-Polanyi equation [9,10]:

$$k = \frac{k_B T}{h} \exp\left(\frac{-\Delta G^{\ddagger}}{RT}\right) \tag{S.23}$$

where k_B is the Boltzmann constant, h is Planck's constant, R is the universal gas constant, and $\Delta G^{\ddagger}$ is the activation free energy. Eq. S.23 can be expanded in terms of activation enthalpies ($\Delta H^{\ddagger}$) and activation entropies ($\Delta S^{\ddagger}$):

$$k = \frac{k_B T}{h} \exp\left(\frac{-\Delta H^{\ddagger}}{RT}\right) \exp\left(\frac{\Delta S^{\ddagger}}{R}\right) \tag{S.24}$$

and then linearized as follows:

$$\ln\left(\frac{k}{T}\right) - \ln\left(\frac{k_B}{h}\right) = -\frac{-\Delta H^{\ddagger}}{RT} + \frac{\Delta S^{\ddagger}}{R} \tag{S.25}$$

Apparent first-order and zero-order activation parameters for methanol dehydration on isolated H^+ sites in CHA zeolites are listed in Table S.2.

Table S.2. First-order, zero-order, and inhibition apparent activation enthalpies ($\Delta H^{\ddagger}$), entropies ($\Delta S^{\ddagger}$), and Gibbs free energies ($\Delta G^{\ddagger}$) measured on CHA with only isolated H^+ sites (383-415 K).

	$\Delta H^{\ddagger}$ / kJ mol^{-1}	$\Delta S^{\ddagger}$ / J mol^{-1} K^{-1}	$\Delta G^{\ddagger}$(415 K) / kJ mol^{-1}
First-order	61	-95	100
Zero-order	115	-7	117
Inhibition	50	-280	165

Rates of methanol dehydration were also measured at elevated temperatures on CHA with only isolated Al sites (up to 473 K, Fig. 7a) and are shown here without a logarithmic pressure scale (Fig. S.14).

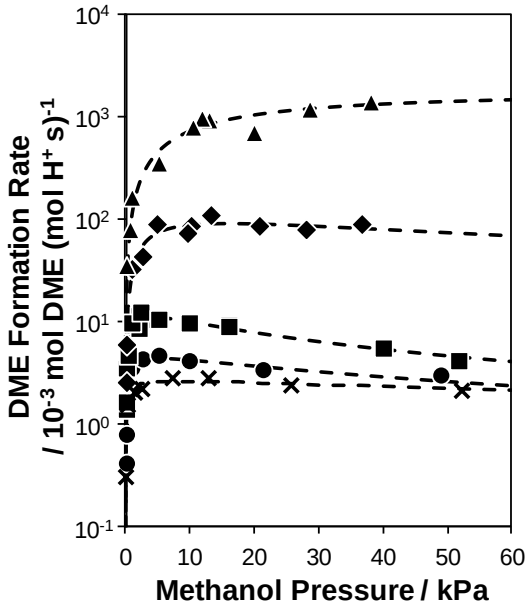

Figure S.15. DME formation rates (per H^+) measured at 398 K (crosses), 403 K (circles), 415 K (squares), 433 K (diamonds), and 473 K (triangles) as a function of temperature (403-473 K) on CHA with only isolated H^+ sites.

DME formation rates (per H^+) were also measured on a CHA zeolite containing 24% paired H^+ sites as a function of temperature (403-473 K) and high-pressure inhibition was also observed to become attenuated at elevated reaction temperatures (>433 K, Fig. S.15).

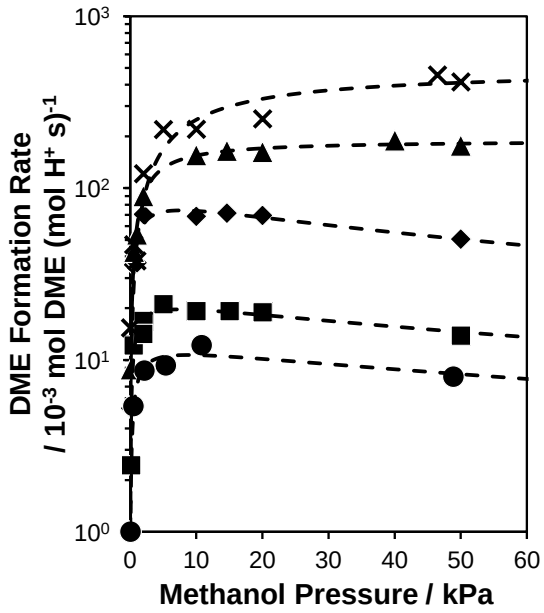

Figure S.16. DME formation rates (per H^+) measured at 403 K (circles), 415 K (squares), 433 K (diamonds), 450 K (triangles), and 473 K (crosses) as a function of temperature (403-473 K) on CHA with 24% paired H^+ sites.

An interesting observation is that high-pressure inhibition appears to become more severe with increasing temperature in the low temperature regime (383-415 K; Fig. S.12), but disappears with increasing temperature above 433 K (Fig. 7a). At low-temperatures (<415 K), both apparent first-order and zero-order rate constants follow an Arrhenius dependence on temperature (383-415 K; Fig. S.13), and the same is true for the apparent inhibition rate constant extracted using Eq. 4 in the main text (Fig. S.14). There does appear to be an outlier in this data set (398 K; Fig. S.14), but removal of this data point does not change the magnitude of the calculated activation enthalpy or entropy substantially (<20% variation). The values of $\Delta H_{inhibit}$ and $\Delta S_{inhibit}$ (Table S.2) suggest that the inhibition is governed largely by entropic penalties likely due to the disruption of partially-ordered methanol structures that form at low-temperatures (<415 K; Fig. 15, main text) and this manifests in more severe inhibition with increasing temperature under these conditions (<415 K), as is observed in Fig. S.12. The formation of larger methanol clusters from gaseous methanol becomes less favorable with increasing temperature (Fig. 11, main text; Section S.15, SI) due to the entropic penalty required for confining multiple methanol molecules within the pores of CHA zeolites. As a result, the surface coverage shifts from a trimer and tetramer covered surface to a monomer and dimer covered surface at elevated reaction temperature (>433 K). This diminished presence of larger methanol clusters at elevated temperatures (>433 K) manifests itself in the disappearance of rate inhibition at high methanol partial pressures (>20 kPa) and gives rise to the trend observed in Fig. 7a of the main text. Ultimately, the trends observed at high methanol pressures (>20 kPa) and increasing temperature (383-473 K) can be rationalized by a trade-off in difference in the entropic barriers for the formation of large adsorbed methanol clusters from gaseous methanol (e.g., trimers and tetramers) and the formation of the dehydration transition state from such clusters.

S.11. Methanol adsorption isotherm on a CHA zeolite

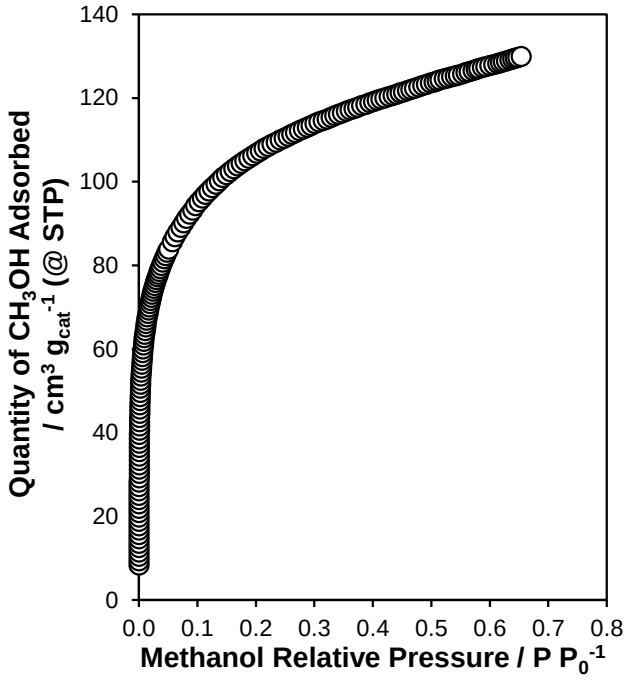

Figure S.17. Methanol adsorption isotherm measured at 293 K as a function of methanol relative pressure on isolated H^+ sites in CHA.

A methanol adsorption isotherm was also measured on a purely siliceous CHA zeolite for comparison and is shown in Fig. S.18. The relative methanol pressure required to adsorb ~10 cm^3 g_{cat}^{-1} (@STP) of methanol on Si-CHA compared to CHA containing only isolated H^+ sites is nearly 4 orders of magnitude larger ($5x10^{-2}$ vs. $6.8x10^{-6}$ P P_0^{-1}), suggesting that these dispersive interactions are significantly weaker than the interactions between methanol and H^+ sites or other adsorbed methanol molecules.

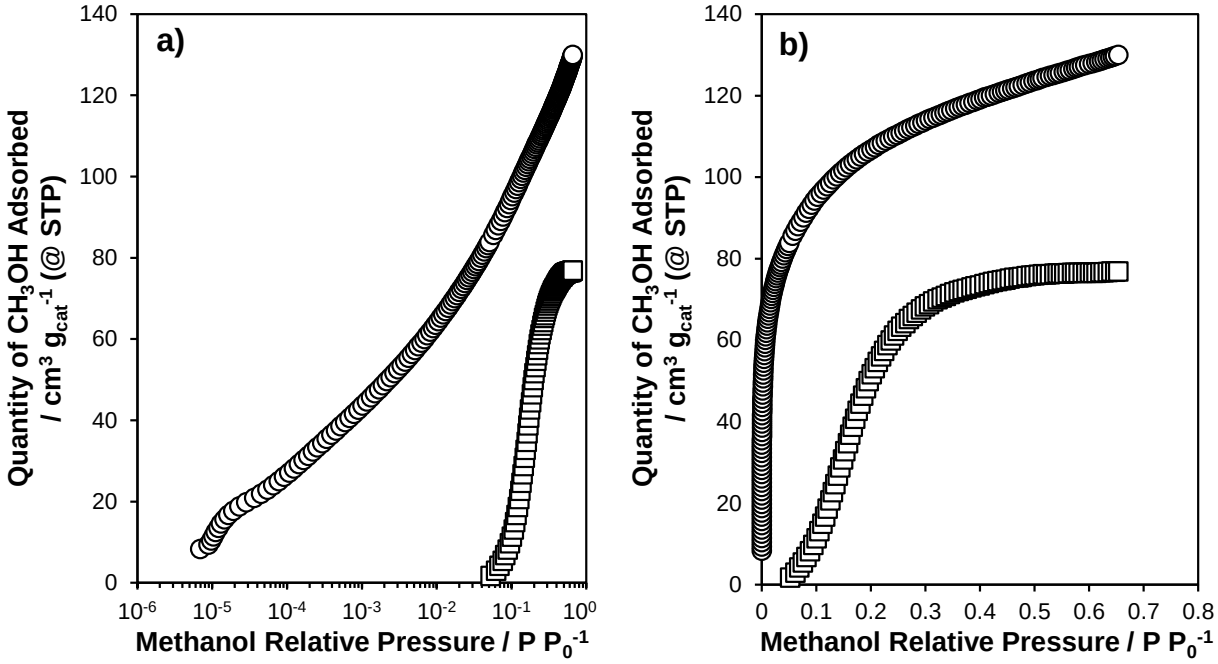

Figure S.18. Methanol adsorption isotherm measured at 293 K on a purely siliceous CHA zeolite (squares) and on an aluminosilicate CHA containing only isolated H^+ sites (Si/Al = 15; circles) as a function of a log (a) and linear (b) relative pressure scale.

S.12. Estimation of methanol conversion as a function of space velocity

Reversible dehydration of surface methoxy species relevant to the dissociative dehydration mechanism gives rise to a rate expression that is predicted to show a strong dependence on methanol conversion (Eq. 7, main text). Methanol conversions were estimated as a function of residence time (mol H^+ s (mol $CH_3OH)^{-1}$) for Eq. 7 using the packed bed differential equation:

$$\frac{\partial X_M}{\partial W} = \frac{1}{F_{M_0}} \frac{k_{DME,D} K_{MMe} K_{Me} P_{CH_3OH} P_{H_2O}^{-1}}{1 + K_D P_{CH_3OH}} \tag{S.26}$$

where X_M is the methanol conversion, F_{M0} is the inlet CH_3OH molar flow rate, the integrand is the rate expression from Eq. 7, and W is the total weight of catalyst to be integrated over. The partial pressure of methanol and water at a given position along the catalyst bed (W) were calculated in terms of conversion as follows:

$$P_{CH_3OH} = \frac{F_{M_0}}{F_{tot}}(1 - X_M) \tag{S.27}$$

$$P_W = \frac{F_{M_0}}{F_{tot}}\left(\frac{X_M}{2}\right) \tag{S.28}$$

where F_{M0} is the initial methanol molar flow rate entering the catalyst bed. The dehydration rate and equilibrium constants were fixed such that the methanol conversion predicted by Eq. S.26 was the same as that measured experimentally (Fig. 2) at a residence time of 3.7 mol H^+ s (mol $CH_3OH)^{-1}$. The differential equation was then solved over a range of residence times (0.01-15 mol H^+ s (mol $CH_3OH)^{-1}$) at 1 kPa of methanol using the same catalyst weight as used to measure the experimental data and is shown in Fig. 2. This qualitative prediction shows a function that bends over sharply with increasing residence time and deviates substantially from the experimentally measured linear dependence of methanol conversion on residence time.

S.13. Derivation of alternative methanol dehydration rate expressions

S.13.1 Kinetically-relevant methoxy formation with empty H^+ sites as a MASI

Rates of DME formation via the dissociative pathway (Scheme 1, main text) can also proceed through methanol monomer dehydration to form surface methoxy as the kinetically-relevant step, with all preceding steps quasi-equilibrated and assuming this step to be irreversible, the rate expression can be described as:

$$r_{D1} = k_{DME,D}[M*] \tag{S.29}$$

where $k_{DME,D}$ is the methoxy formation rate constant and [M*] is the concentration of methanol monomers on the surface. Considering the adsorption of gaseous methanol, at a given partial pressure (P_{CH3OH}), at an empty H^+ site ([*]) to form methanol monomers to be quasi-equilibrated:

$$K_M = \frac{[M*]}{P_{CH_3OH}[*]} \tag{S.30}$$

we can substitute Eq. S.30 into Eq. S.29 to get the rate of DME formation in terms of measureable quantities:

$$r_{D1} = k_{DME,D}K_M P_{CH_3OH}[*] \tag{S.31}$$

Assuming that empty H^+ sites, methanol monomers, and protonated dimers (given by [D*]), which are considered to be inhibitory species for the dissociative pathway, are the most abundant surface intermediates (MASI) during methanol dehydration catalysis, the total number of sites [L] can be expressed as:

$$[L] = [*] + [M*] + [D*] \tag{S.32}$$

Taking protonated dimers to be in quasi-equilibrium with methanol monomers and a gaseous methanol:

$$K_D = \frac{[D*]}{P_{CH_3OH}[M*]} \tag{S.33}$$

Eq. S.32 can be rewritten as:

$$[L] = [*] + K_M P_M[*] + K_D K_M P_{CH_3OH}^2[*] \tag{S.34}$$

Solving for the total number of empty H^+ sites:

$$[*] = \frac{[L]}{1+K_M P_{CH_3OH}+K_D K_M P_{CH_3OH}^2} \tag{S.35}$$

and substituting Eq. S.35 into Eq. S.31 gives the resulting rate expression for DME formation from kinetically-relevant methoxy formation:

$$r_{D1} = \frac{k_{Me}K_M P_{CH_3OH}}{1+K_M P_{CH_3OH}+K_M K_D P_{CH_3OH}^2} \tag{S.36}$$

IR spectra measured during steady-state methanol dehydration catalysis (0.1-22 kPa, 415 K) indicate that all H^+ sites are covered by methanol during catalysis [11]. This eliminates empty H^+ sites as a possible MASI and reduces Eq. S.35 to:

$$[*] = \frac{[L]}{K_M P_{CH_3OH}+K_D K_M P_{CH_3OH}^2} \tag{S.37}$$

This ultimately eliminates the numerator of Eq. S.36 and generates the following function that is always -1 order in methanol under all conditions:

$$r_{D1} = \frac{k_{Me}}{1+K_D P_{CH_3OH}} \tag{S.38}$$

S.13.2 Kinetically relevant DME formation considering reversible methoxy formation

Another alternative rate law can be derived from kinetically-relevant DME formation, but considering methoxy formation to be reversible and quasi-equilibrated. Considering DME formation as the kinetically-relevant step, the rate expression becomes:

$$r_{D2} = k_{DME,D}[MMe*] \tag{S.39}$$

where, [MMe*] is the concentration of methoxy/methanol co-adsorbed species on the surface (Scheme 1, main text). If we consider the formation of methoxy/methanol co-adsorbed species (Eq. S.40), dehydration to form surface methoxy (Eq. S.41), and methanol adsorption to form methanol monomers (Eq. S.42) to be quasi-equilibrated:

$$K_{MMe} = \frac{[MMe*]}{P_{CH_3OH}[Me*]} \tag{S.40}$$

$$K_{Me} = \frac{[Me*]P_{H_2O}}{[M*]} \tag{S.41}$$

$$K_M = \frac{[M*]}{P_{CH_3OH}[*]} \tag{S.42}$$

Eq. S.39 can now be rewritten in terms of measurable quantities:

$$r_{D2} = k_{DME,D}K_{MMe}K_{Me}P_{CH_3OH}^2 P_{H_2O}^{-1}[*] \tag{S.43}$$

Based on IR spectra taken during methanol dehydration catalysis [11], we will consider the MASI to be methanol monomers and protonated dimers, which allows us to write the total number of sites, [L], as:

$$[L] = [M*] + [D*] \tag{S.44}$$

Solving for the number of vacant sites yields Eq. S.37, which can then be substituted into Eq. S.43 to give:

$$r_{D2} = \frac{k_{DME,D}K_{MMe}K_{Me}P_{CH_3OH}P_{H_2O}^{-1}}{1+K_D P_{CH_3OH}} \tag{S.45}$$

S.14. Maximum rate analysis of DFT-predicted DME formation rates

Parallel pathways contribute to overall dimethyl ether (DME) formation rates when transition states with spectating methanol molecules are considered. Therefore, the rates of DME formation are described by a sum of these parallel rates. As shown in Section S.3., methoxy formation is the kinetically-relevant step in the dissociative route. Therefore, the observed rate of DME formation is

$$r_{obs} = \sum_{i=1}^{4} r_{D1,i} + \sum_{j=2}^{4} r_{A,j} \quad \text{(S.46)}$$

where i and j represent the total methanol molecules participating in the dissociative and associative route, respectively. This sum represents the experimentally observed DME formation rate

$$r_{obs} = \frac{\sum_{i=1}^{4} \alpha_i P_{CH_3OH}^{i} + \sum_{j=2}^{4} \beta_j P_{CH_3OH}^{j}}{\sum_{m=1}^{5} K_m P_{CH_3OH}^{m}} \quad \text{(S.47)}$$

where α_i and β_j represent apparent rate coefficients for the first step of the dissociative route with i total methanol molecules and the associative route with j total methanol molecules, respectively, and K_m represents a lumped equilibrium constant for the formation of a cluster of m methanol molecules.

S.15. DFT-calculated structures of methanol clusters

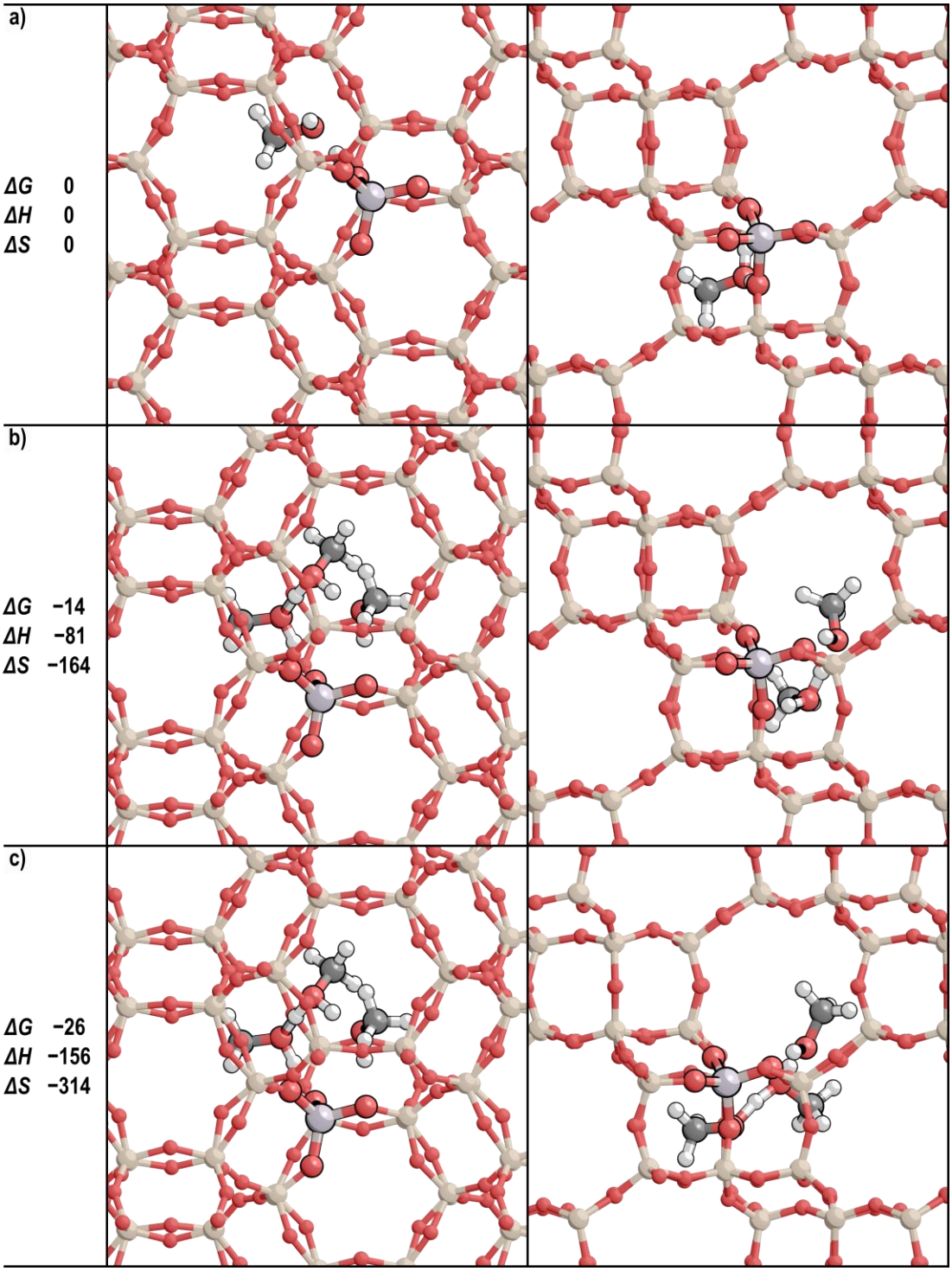

Figure S.19. The most stable methanol clusters shown with views along the c-axis of the CHA unit cell (left) and along the b-axis of CHA (right) with (a) one, (b) two, and (c) three methanol molecules. Free energies (ΔG) and enthalpies (ΔH) in kJ mol^{-1}, and entropies (ΔS) in J mol^{-1} K^{-1}, are shown relative to the methanol monomer at 415 K and 1 bar CH_3OH.

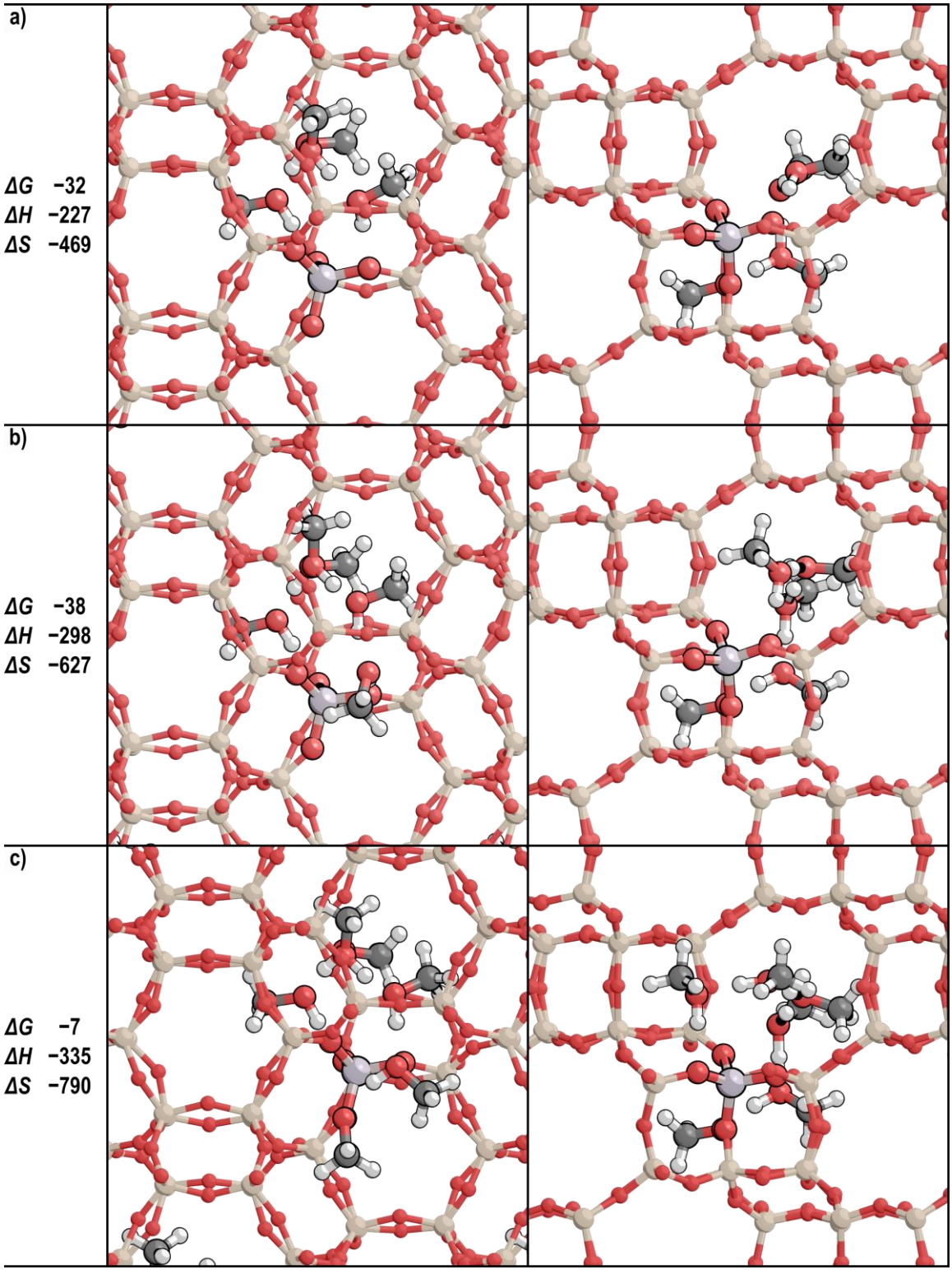

Figure S.20. The most stable methanol clusters with views along the c-axis of the CHA unit cell (left) and along the b-axis of CHA (right) with (a) four, (b) five, and (c) six methanol molecules. Free energies (ΔG) and enthalpies (ΔH) in kJ mol^{-1}, and entropies (ΔS) in J mol^{-1} K^{-1}, are shown relative to the methanol monomer at 415 K and 1 bar CH_3OH.

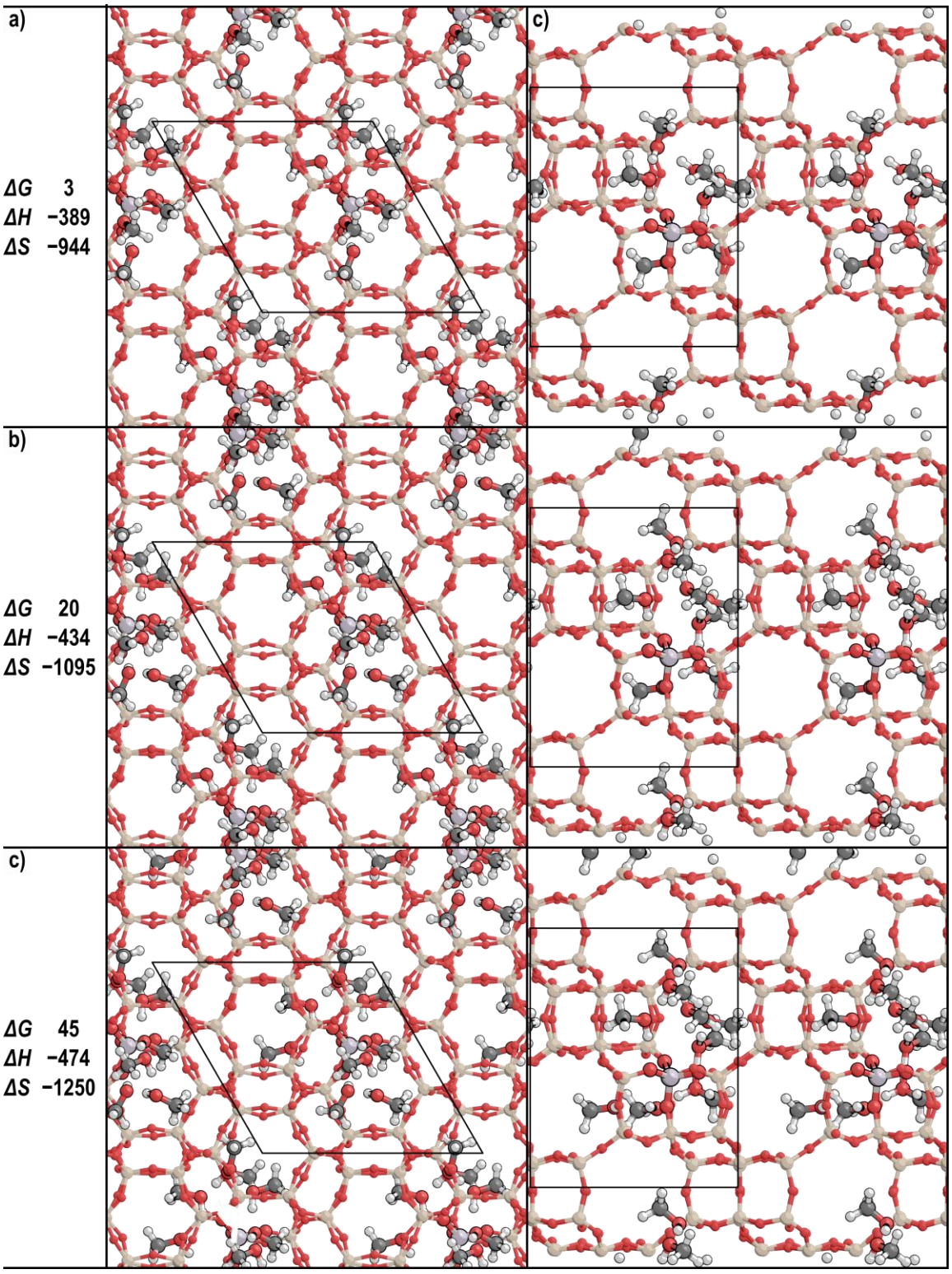

Figure S.21. The most stable methanol clusters with views along the c-axis of the CHA unit cell (left) and along the b-axis of CHA (right) with (a) seven, (b) eight, and (c) nine methanol molecules. Free energies (ΔG) and enthalpies (ΔH) in kJ mol^{-1}, and entropies (ΔS) in J mol^{-1} K^{-1}, are shown relative to the methanol monomer at 415 K and 1 bar CH_3OH.

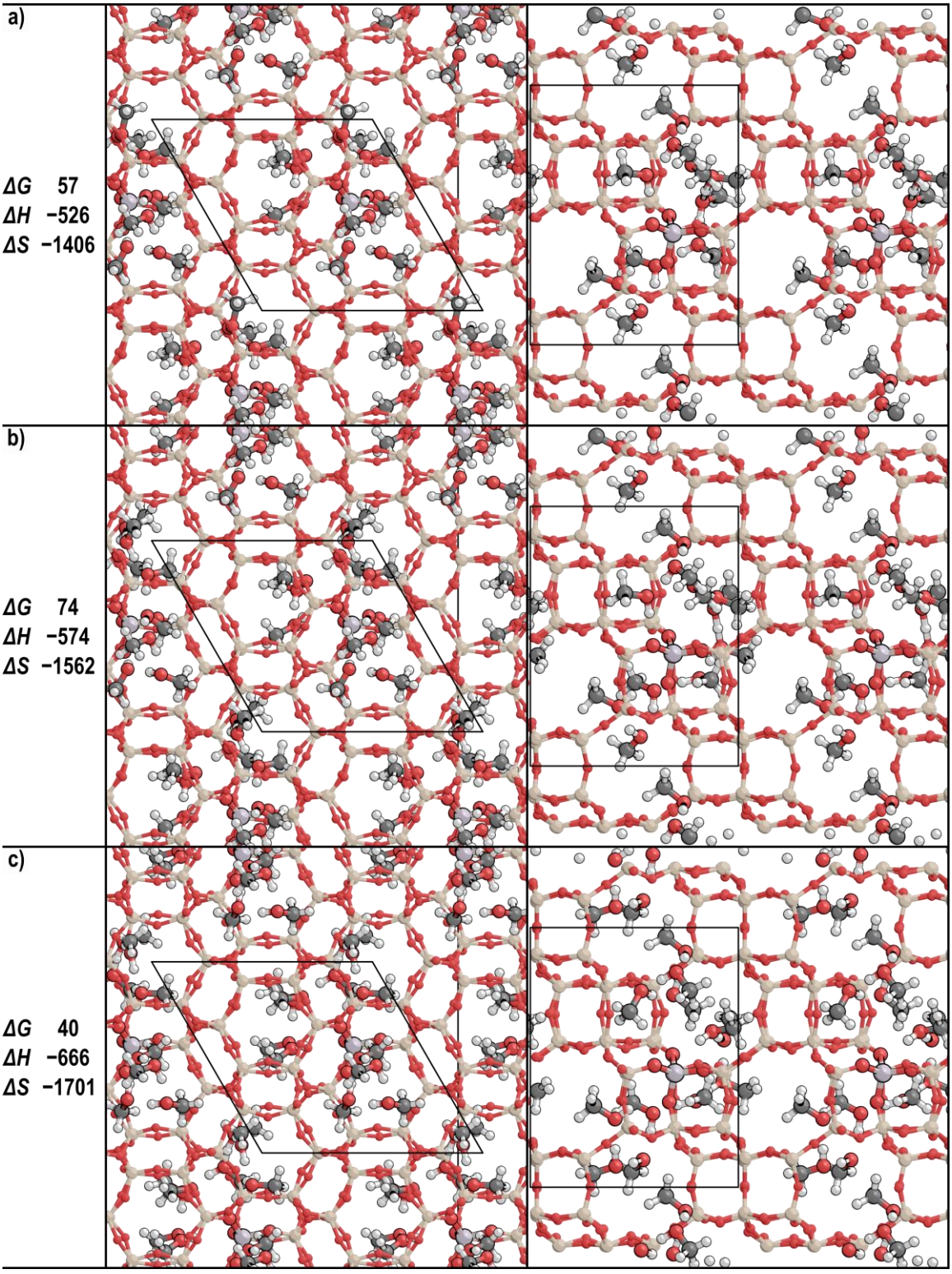

Figure S.22. The most stable methanol clusters with views along the c-axis of the CHA unit cell (left) and along the b-axis of CHA (right) with (a) ten, (b) eleven, and (c) twelve methanol molecules. Free energies (ΔG) and enthalpies (ΔH) in kJ mol^{-1}, and entropies (ΔS) in J mol^{-1} K^{-1}, are shown relative to the methanol monomer at 415 K and 1 bar CH_3OH.

S.16. Derivation of methanol Gibbs free-energies

Values of the methanol Gibbs free energy were calculated as a function of methanol pressure and temperature to relate adsorption equilibrium between gaseous methanol and adsorbed methanol under different conditions. Methanol adsorbed within the pores of CHA was considered to be similar to liquid methanol, due to the presence of methanol clusters in IR spectra (~3370 cm^{-1}) measured during methanol dosing experiments (Fig. 10, main text) and during steady-state methanol dehydration catalysis [11]. The vibrational band attributed to methanol clusters represents perturbed H-bonding interactions between adjacent methanol molecules that are assumed to be more similar in structure to liquid methanol than to gaseous methanol. While this assumption does not account for strong interactions between methanol monomers and bare H^+ sites or for stabilization via van der Waals interactions with the framework, it does provide an initial approximation of methanol coverage within CHA under reaction conditions (>0.01 kPa CH_3OH, 415 K). DFT calculations, which are able to rigorously account for differences in the adsorption free energy of different sized methanol clusters and for interactions between adsorbed methanol with the zeolite framework, predict methanol coverages similar to those estimated by assuming equilibrium with an ideal liquid-like adsorbed methanol (Fig. 11, main text).

Equilibrium between gaseous methanol and adsorbed, liquid-like methanol occurs when the chemical potential (μ) of both states are equal:

$$\mu_m = \mu_{m*} \tag{S.48}$$

where μ_m is the chemical potential of gaseous methanol and μ_{m*} is the chemical potential of adsorbed methanol. Here changes in free energy of the zeolite lattice upon adsorption of methanol are assumed to be negligible. The chemical potential of a species, i, can then be expressed as the sum of the ideal state (μ^0) and the excess chemical potential (μ^ε):

$$\mu_i = \mu_i^0 + \mu_i^\varepsilon \tag{S.49}$$

where μ^ε of species i (μ_i^ε) can be expressed in terms of the activity of species i (a_i):

$$\mu_i^\varepsilon = RT\ln[a_i] \tag{S.50}$$

Substituting Eq. S.49 and S.50 into S.48 yields:

$$\mu_m^0 + RT\ln[a_m] = \mu_{m*}^0 + RT\ln[a_{m*}] \tag{S.51}$$

Estimation of the gas-phase methanol activity coefficient (γ_M) at 415 K using the Peng-Robinson equation of state gives activity coefficients near unity (γ_M>0.98), indicating that under the conditions studied here (415 K, 0.01-50 kPa CH3OH), gas-phase methanol behaves as an ideal gas. As a result, a_m can be rewritten as:

$$a_m = \frac{P_m}{P_0} \tag{S.52}$$

where P_m is the partial pressure of methanol and P_0 is a reference pressure of 1 bar. The activity of the adsorbed methanol phase was considered by treating adsorbed methanol as a pure-component liquid, in order to approximate the equilibrium between gaseous and adsorbed methanol. The

activity of adsorbed methanol can be written in terms of the fugacity of adsorbed methanol (f_{m*}) at a given T and P:

$$a_{m*} = \frac{f_{m*}}{f^0_{m*}} \tag{S.53}$$

where f^0_{m*} is the fugacity of methanol under a reference condition of 1 bar. The fugacity of adsorbed liquid-like methanol can then be related to a saturated liquid using a Poynting factor:

$$f_{m*} = \varphi^{sat}_{m*} P^{sat}_{m*} \exp\left[\frac{v_{m*}}{RT}(P - P^{sat}_{m*})\right] \tag{S.54}$$

and at low pressures, the Poynting factor approaches unity and by considering adsorbed methanol as an ideal liquid, Eq. S.54 reduces to:

$$f_{m*} = P^{sat}_{m*} \tag{S.55}$$

Eq. S.53 can now be rewritten in terms of P^{sat}_{m*}, referenced to a pressure of 1 bar:

$$a_{m*} = \frac{P^{sat}_{m*}}{P_0} \tag{S.56}$$

Rearranging Eq. S.51 and substitution of Eq. S.52 and S.56 yields:

$$\mu^0_{m*} - \mu^0_m = RT\ln\left[\frac{P_m}{P_0}\right] - RT\ln\left[\frac{P^{sat}_{m*}}{P_0}\right] \tag{S.57}$$

Assuming a constant T and P process, the change in the chemical potential can then be rewritten in terms of the change in Gibbs free energy (per mole) and results in Eq. 9 of the main text:

$$\Delta G_m = RT\ln\left[\frac{P_m}{P^{sat}_{m*}}\right] \tag{S.58}$$

Eq. S.58 provides an estimation of the difference in free energy between adsorbed methanol and gaseous methanol as a function of temperature and pressure. This equation was then used to calculate the free energy of methanol at different partial pressures during methanol adsorption isotherms (293 K) and under reaction conditions (415 K) to estimate the coverage of methanol during methanol dehydration catalysis (Fig. 9, main text).

S.17. Complete methanol dehydration reaction network

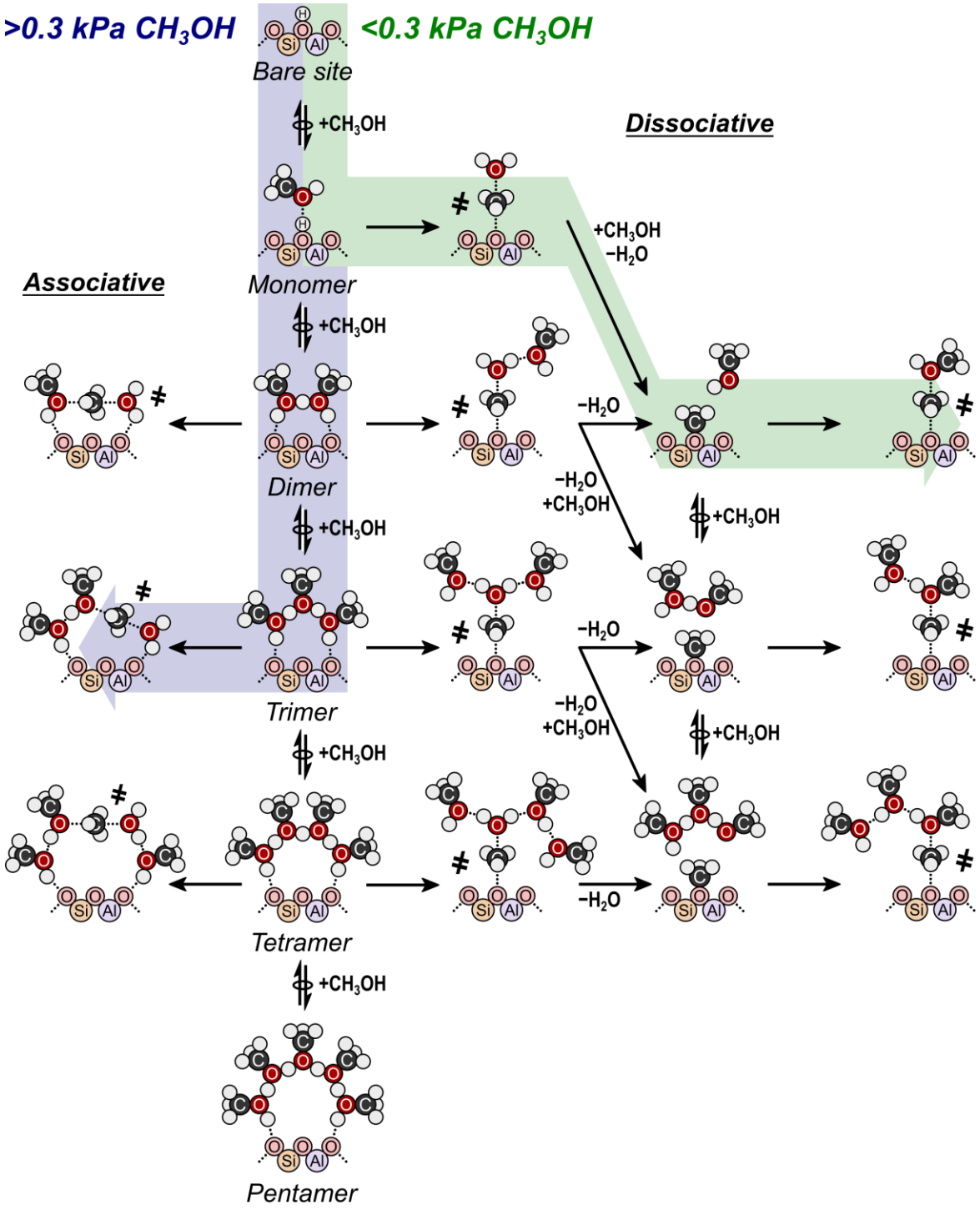

Scheme S.4. Complete methanol dehydration reaction network for the associative and dissociative dehydration mechanisms as a function of methanol coverage. The most favorable reaction pathway for methanol pressures <0.3 kPa and >0.3 kPa are highlighted in green and blue, respectively, and correspond to the maximum rate analysis presented in Figure 16 of the main text.

S.18. References

[1] D.A. McQuarrie, Statistical mechanics, University Science Books, Sausalito, Calif, 2000.

[2] C. Baerlocher, L.B. McCusker, Database of Zeolite Structures: http://www.iza-structure.org/databases., (2013). http://www. iza-structure. org/databases (accessed January 5, 2017).

[3] S. Nystrom, A. Hoffman, D. Hibbitts, Tuning Brønsted acid strength by altering site proximity in CHA framework zeolites, ACS Catal. 8 (2018) 7842–7860. doi:10.1021/acscatal.8b02049.

[4] M. DeLuca, P. Kravchenko, A. Hoffman, D. Hibbitts, Mechanism and Kinetics of Methylating C_6 –$C1_2$ Methylbenzenes with Methanol and Dimethyl Ether in H-MFI Zeolites, ACS Catal. 9 (2019) 6444–6460. doi:10.1021/acscatal.9b00650.

[5] A. Ghorbanpour, J.D. Rimer, L.C. Grabow, Computational Assessment of the Dominant Factors Governing the Mechanism of Methanol Dehydration over H-ZSM-5 with Heterogeneous Aluminum Distribution, ACS Catal. 6 (2016) 2287–2298. doi:10.1021/acscatal.5b02367.

[6] R.T. Carr, M. Neurock, E. Iglesia, Catalytic consequences of acid strength in the conversion of methanol to dimethyl ether, J. Catal. 278 (2011) 78–93. doi:10.1016/j.jcat.2010.11.017.

[7] W. Song, D.M. Marcus, H. Fu, J.O. Ehresmann, J.F. Haw, An oft-studied reaction that may never have been: direct catalytic conversion of methanol or dimethyl ether to hydrocarbons on the solid acids HZSM-5 or HSAPO-34., J. Am. Chem. Soc. 124 (2002) 3844–3845. doi:10.1021/ja016499u.

[8] S. Chen, E.I. Izgorodina, Prediction of 1H NMR chemical shifts for clusters of imidazolium-based ionic liquids., Phys. Chem. Chem. Phys. 19 (2017) 17411–17425. doi:10.1039/c7cp02951a.

[9] H. Eyring, The Activated Complex in Chemical Reactions, J. Chem. Phys. 3 (1935) 107. doi:10.1063/1.1749604.

[10] M.G. Evans, M. Polanyi, Some applications of the transition state method to the calculation of reaction velocities, especially in solution, Trans. Faraday Soc. 31 (1935) 875. doi:10.1039/tf9353100875.

[11] J.R. Di Iorio, C.T. Nimlos, R. Gounder, Introducing Catalytic Diversity into Single-Site Chabazite Zeolites of Fixed Composition via Synthetic Control of Active Site Proximity, ACS Catal. 7 (2017) 6663–6674. doi:10.1021/acscatal.7b01273.